Title: Electron diffraction captures high-resolution structures from *in vivo* protein nanocrystals of *Bacillus thuringiensis*

Authors: Marcus Gallagher-Jones[1*], Robert Bücker[2,3], Quentin Delaunay[4], Nicolas Coquelle[4], Elena A. Andreeva[4,5], Angharad Smith[1,6], Ninon Zala[4], Paul Montmayeul[4], R. J. Dwayne Miller[6,7], Judy S. Kim[1,8], Angus I. Kirkland[1,8] & Jacques-Philippe Colletier[4*]

Affiliations:
[1]The Rosalind Franklin Institute, Didcot, OX11 0QS, UK;
[2]Max Planck Institute for the Structure and Dynamics of Matter, CFEL, 22761, Hamburg, Germany;
[3]Rigaku Corporation, Akishima, Tokyo 198-8666, Japan;
[4]Univ. Grenoble Alpes, CNRS, CEA, Institut de Biologie Structurale, Grenoble, F-38000, France;
[5]Department of Biomolecular Mechanisms, Max Planck Institute for Medical Research, 69120 Heidelberg, Germany
[6]School of Chemistry, University of Leeds, Leeds, UK
[7]Departments of Chemistry and Physics, University of Toronto, ON M5S 3H6, Canada.
[8]University of Oxford, Department of Materials, , Parks Road, Oxford, OX13PH, UK
*correspondance email: marcus.gallagher-jones@rfi.ac.uk
jacques-Philippe.Colletier@ibs.fr

Authors contributions: MGJ, RJDM, JSK, AIK and JPC designed the project; QD, EAA, NZ and PM expressed and purified protein crystals; QD collected SEM images; MGJ, RB and AS vitrified samples for CryoEM studies; MGJ collected CryoTEM images; MGJ and AS performed 3DED data collection; RB, QD and MGJ performed SerialED data collection; RB, JPC and NC performed SerialED data analysis; MGJ and JPC performed 3DED data analysis, structural analysis and wrote the manuscript with inputs from all authors.

Abstract (152 words)

Bacillus thuringiensis is one of the most widely used biopesticides worldwide owing to the highly specific pesticidal-proteins various strains produce in the form of nanocrystals. Structure determination of such crystals remains difficult because their small size makes them unsuitable for conventional X-ray crystallography. Here we explore two emerging (cryo-) electron diffraction techniques, namely three-dimensional electron diffraction and serial electron diffraction, as tools for studying the structures of these crystals. Using the mosquitocidal protein Cry11Aa as an example, we compare electron diffraction with state of the art results obtained with an X-ray free electron laser. Our work demonstrates that electron diffraction is a viable alternative for structure determination from such challenging crystals, in some cases outperforming previous results obtained with X-ray free electron lasers. We present a workflow based on readily available instrumentation enabling structure

determination directly from the crystals grown *in vivo*, unperturbed by dissolution and therefore preserved in their native state.

Introduction (1004 words)

The bacterium *Bacillus thuringiensis* (*Bt*) produces in the form of naturallyoccurring nanocrystals a variety of pesticidal proteins[1,2]. These are used worldwide to control agricultural pests and insect vector populations in an environmentally sound fashion[3,4]. The intracellular growth of the crystals is limited by the boundary of the *Bt* cell membrane, explaining their sub-micron size. The overall mechanism of action of these crystalline proteins lies in their ingestion by insect (or nematode) larvae[5], in the gut of which the crystals dissolve upon alkaline (or acidic) activation, releasing constitutive proteins that are then activated proteolytically transforming them into a transmembrane pore[6], generally upon interaction with a receptor (Cry and Tpp proteins) or the lipidic bilayer (Cyt proteins)[7,8]. Detailed information of the structure-function relationships of these proteins, and notably how the bio-activation takes place, remains incomplete. This is due to the small size of the natural crystals, which makes them unsuited for structure determination by oscillation-based cryo-crystallography at synchrotron light sources. Indeed, their limited number of unit-cells translates to both weak diffraction-signal arising from each crystal and high sensitivity to radiation damage. To circumvent this barrier, investigators initially resorted to crystallization of heterologously-expressed protein or dissolution of the natural crystals followed by proteolytic activation and re-crystallisation[9,10]. This strategy has been successful for a limited number of *Bt* proteins[11–13], but in doing so, information was lost regarding the native crystal packing as it could not be assumed that the latter would be preserved in the re-crystallisation process; more so when proteins were proteolytically activated prior to this step. However, the way in which the proteins pack in the crystal is central to understanding the biological activation cascade of these proteins[14]. The ideal method would be to solve these protein structures directly from the natural crystals produced by *Bt*. To date, with one exception[15], this has been attained only using serial femtosecond crystallography (SFX) at X-ray free electron lasers (XFELs), where ultra-short, highly-intense (sub)-µm-focused X-ray pulses can be used to decouple the resolution of recordable diffraction from radiation damage[16]. Using SFX, structures could be solved of half a dozen naturally crystalline pesticidal proteins which, despite wide spread application, lacked proper structural characterisation. These include *Bacillus thuringiensis* (*Bt*) Cry3Aa[17], Cyt1Aa[14], Cry11Aa and Cry11Ba[18], as well as *Lysinibacillus shaericus* Tpp49Aa[19] and the binary complex formed by Tpp1Aa2 and Tpp2Aa2 (formerly known as BinAB)[20]. With the aim to control crystal properties, and thereby better their pesticidal activity, many of these studies pursued insights into the protein dynamics that govern crystal dissolution[14,18,20]. It was shown that mutation of residues at select interfaces (effectively changing a single atom over 2700 to 8000) can affect the shape or size of crystals, their dissolution properties, as well as their pesticidal activity[14,18,20]. These results demonstrate the value of determining *Bt* nanocrystalline

protein structures as they naturally occur, with the goal of understanding their biological activation cascades. However, SFX still presents two weaknesses. Firstly, the method has a high rate of sample consumption, as not only is each crystal impinged once, but at most 0.000000001 % of them actually see the beam owing to the combination of the shortness of the pulses (5-40 fs) with the XFEL repetition rate (30-2700 Hz) amounting to the beam being available for ~0.02 to 0.1 ns/s[21]. Notably, in all of the studies above, a liquid jet was used to present samples to the beam, which requires a large amount of sample (1-4 hour injection of a slurry at 0.1-0.5 x10^9 crystals/ml flown at 1-15 µl/min), despite compression of the jet by pressured gas[22] (gas-dynamic virtual nozzle ; 6-10 µm jet) or nanoflow electrospinning[23,24] (0.1-0.2 µm jet). Secondly, XFEL beamtime is being increasingly attributed to projects seeking to unveil ultra-short timescale structural-dynamics, underpinning e.g. redox reactions, photo-induced isomerization and cleavage, or excited state proton and electron transfers[25–27]. The continuation of structural biology research on *Bt* pesticidal proteins therefore requires the development of alternative methods for structure determination.

Electron diffraction (ED) techniques, such as 3D electron diffraction (3DED)[28,29], are promising alternatives for the study of nanocrystals. In these methods, sometimes referred to as microcrystal electron diffraction (MicroED)[30,31], diffraction data are recorded continuously as the crystal is oscillated in the electron beam, in a manner analogous to conventional (oscillation-based) X-ray crystallography[32]. Owing to the greater interaction cross-section and more favourable ratio of elastic to inelastic scattering events of electrons compared to X-rays[33], meaningful data can be captured from substantially smaller crystals, as illustrated by the hundreds of structures now solved of small molecules[34–36], peptides[37–39] and proteins[40–42]. In practice, determination of peptide and protein structures requires vitrification of crystalline sample at cryogenic temperatures, to mitigate the progression of radiation damage[43]. This increases the lifetime of crystals in the electron beam and thereby allows collection of a partial dataset prior to sample degradation, which can be indexed, and then scaled and merged to other partial datasets, in the end affording structure determination using conventional (X-ray) crystallography software[31], based on the merged (and thereby complete) dataset. Most recently, scanning electron diffraction methods such as 4DSTEM and SerialED have emerged as alternative approaches to capturing electron diffraction data[44]. In these, a near parallel beam is scanned to collect still diffraction patterns in a serial fashion and from tens of thousands of localised grid positions. These techniques are hindered by the flatness of the Ewald sphere associated with the typically-used electron wavelengths (~0.02 Å), leaving 3D information mostly absent from the diffraction pattern. As such the indexing of crystal-hits is reliant on the availability of prior crystal symmetry information. Scanning ED techniques have been applied to lysozyme and granulovirus inclusions[45] as well as radiation sensitive zeolites[46]

and peptides[47]. For the proteinaceous samples, the recorded resolution surpassed that achieved by SFX, highlighting the potential of these approaches in protein nanocrystallography.

Here, we have used 3DED and SerialED as tools for determining structures from naturally-occurring crystals of *Bt* pesticidal proteins. The structure of the mosquitocidal protein Cry11Aa was solved using both methods, and resulting models compared to one another, as well as to that previously obtained by SFX[18]. The potential and limitations of ED were further explored by capturing diffraction data from a variety of *Bt*-grown nanocrystals, including some that had proven too challenging for solution by SFX.

Results (2492 words)

3DED of Cry11Aa

The potential of electron diffraction to solve structures from naturally-occurring *Bt* crystals was first explored by applying 3DED to Cry11Aa. Frozen-hydrated CryoEM grids of isolated crystals were prepared by back-blotting using a 1000-fold dilution of the same crystalline slurry used at the XFEL[18], resuspended in 10% glycerol. We tested several different grid types but found that holey carbon grids give the best distribution of crystals as the variable hole sizes on the grid accommodates the variety of crystal sizes present in solution (Fig. 1a). Sample grids were loaded into an electron microscope operating at 200 kV and 80 K, and the imaging of crystals in TEM mode revealed the presence of a clear lattice suggesting that the crystals could produce high quality diffraction (Fig. 1b, c). Samples were first screened visually in diffraction mode by overfocussing the diffraction pattern to form an image. Crystals were centred within the selected area aperture and the beam was refocussed to form a diffraction pattern. Well diffracting crystals were selected for further rotation data collection. Due to the small number of unit cells per crystal (10^5), and with view to maximise the amount of signal that could be extracted, we opted to record data on a monolithic direct electron detector (Gatan, K2 summit) operating in counting mode[48–50]. Combining a wide-field parallel beam illumination with an 0.8 µm (in object space) selected-area aperture to define the diffracting region, energy-filtered diffraction data were recorded with signal extending as far as 2.3 Å in favourable cases (Fig. 1d). The sensitivity of crystals to radiation damage was apparent, with diffraction fading over the wedge of data collected, irrespective of the selected crystal. Hence, we opted to record a small angular wedge (30 degrees) at a slightly elevated fluence from multiple crystals to maximise the amount of signal at high-resolution. Using this approach, we collected energy-filtered diffraction data from 47 crystals starting from different initial tilt angles, which was necessary to overcome the large variation in diffraction quality of the *in vivo* grown crystals and their preferred orientation on the grids. The quality of data recorded in counting mode was sufficient for unit cell and space group assignment without the need for additional constraints. For consistency, the unit cell derived from the dataset with the best statistics was used as input for indexing and ultimately merging 39 of the 47 datasets to give a final set of reflections at 2.85 Å resolution (Table 1). The overall completeness of the dataset was limited due to a preferred orientation of the plate-like crystals on the EM grid and the limited rotation range of the goniometer. To minimize potential bias arising from the SFX structure, a model generated by Alphafold3[51] was used as a starting point for molecular replacement after trimming of low confidence regions (Supplementary. Fig. 1). After several rounds of iterative building and refinement, the final model contained residues 13 to 643 with a R_{work}/R_{free} of 0.17/0.24 (Table 1). An overlay with the structure solved by SFX showed a high degree of similarity with an all

atom RMSD of 0.79 Å (Fig. 2a). The largest deviations between the structures are seen in the loop (N-ter) and β-turn (C-term) segments adjacent to the protein β-pin (Fig. 2a). This specific β-strand, unseen in Cry proteins other than those belonging to the Cry11 primary group, serves as the dimerization interface (C2 symmetry) between Cry11Aa dimers (C2 symmetry), leading to the formation of tetramers (D2) that are the building block (one per unit cell) for Cry11Aa crystal assembly. Regardless of the used technique, the electron density (SFX) and electrostatic potential (3DED) are well defined for the β-pin itself, but those of the bordering loop (N-ter) and β-turn (C-term) are not, indicating appreciable structural dynamics in these (SFX data collected at 300 K) as well as susceptibility to flash-cooling (3DED data collected at 80 K) (Fig. 2b-d).

Energy-filtering of the diffraction signal was implemented with the aim to reduce the large background caused by inelastic scattering from the bulk solvent (Fig. 3) and in this manner to improve the signal-to-noise ratio (SNR) of the data[52–54]. To verify that this was indeed the case and assess the benefits of energy-filtering for 3DED data collected on *Bt* nanocrystals, we also recorded 29 datasets with the energy-selecting slit completely open, which yielded a merged dataset at 3.73 Å resolution (Table 2). This loss in resolution could be mitigated by excluding datasets where the stage had started from a higher tilt angle, resulting in a merged dataset at 2.99 Å but at a severe penalty to completeness (Table 2). To obtain a better picture of where energy-filtering makes the biggest difference, each of the diffraction datasets was analysed individually, applying the same data quality cutoff of CC½ > 0.3, and data reduction statistics were thereafter compared. We find that the energy filtered data are better in several key indicators including resolution, overall R_{merge} and SNR (Supplementary. Fig. 2). This difference is more pronounced when the starting angle of the stage is far from zero, *i.e.*, when the apparent thickness of the sample is largest. This effect is particularly obvious when looking at I/σ in the low spatial frequencies which suffer greatly from the increased background due to the inelastic scattering of the solvent (Supplementary. Fig. 2d). As the contribution of inelastic scattering is isotropic and predominantly additive, we investigated whether the alternative approach of subtracting the inelastic background would have yielded data of similar quality as those obtained with energy-filtering. We found this approach to be sub-optimal, with the SNR after background subtraction being reduced compared to energy-filtered data (Fig. 3c). This is consistent with previous observations that energy-filtering improves the SNR of ED data generally and at all spatial frequencies[52]. Additionally, as energy-filtering reduces the number of electrons reaching the detector, there should be a reduction in coincidence loss at a given flux for electron counting detectors. This will produce more reliable signal in regions where inelastic scattering is high, for example at lower spatial frequencies.

SerialED of Cry11Aa

The 3DED data were ultimately limited in the highest resolution that could be achieved due to the need to fractionate a fixed electron fluence over multiple frames. In an attempt to ameliorate this, whilst also reducing cumulative damage, we opted to collect electron diffraction data serially, *i.e.*, with a single, high-fluence exposure per crystal and without rotation of the goniometer during data collection[45,55]. For these SerialED experiments, Cry11Aa crystals were vitrified on CryoEM grids in a similar manner as described above, and after loading into the 200 kV STEM equipped with a dedicated diffraction detector[45], a ~110 nm parallel beam was used and data were collected by raster-scanning of the grids, *i.e.*, in a process analogous to serial data collection on solid-supports at an X-ray free electron laser or synchrotron[56–58]. To maximise data collection efficiency, a low-resolution focussed probe darkfield STEM image was first taken of an area of ~300 μm^2 containing 10s to 100s of crystals. Segmentation was performed on this image to automatically map the centroids of each crystal. The microscope was then switched into a parallel nanobeam mode, and a custom scan generator was used to drive the STEM scan coils to position the parallel probe over each crystal. By synchronising this with a hybrid pixel detector with a large dynamic range and fast readout, it was possible to record nearly a thousand of such diffraction patterns per hour. In this manner, we collected 14620 SerialED diffraction patterns from Cry11Aa crystals, of which 12625 could be indexed by CrystFEL (v. 0.10.0+9438abb0)[59] using the pinkIndexer algorithm[60] and intensities were finally merged using a Monte-Carlo approach (Supplementary. Fig. 3). The data were significantly anisotropic (Fig. 4), which questions the validity of the figures of merit calculated based on isotropic resolution shells, indicating a resolution of 2.2 Å. We therefore subjected the merged dataset to Staraniso[61] which, using a local <I/sigI> of 1.2 as the diffraction cutoff criterion, found resolution limits of 2.3, 1.8 and 2.1 Å along the a*, b* and c* directions, and an anisotropy SNR of 27.8. Such an anisotropy of the diffraction was not visible in the SFX data, nor in the data collected using 3DED (Fig. 4), indicating that it is not a property of the crystals but a shortcoming arising from the preferred orientation of crystals on the grid. In the 3DED data, the issue is partly compensated for by rotation of the stage, however a missing wedge in the diffraction plane remains due to the limited rotation range of the goniometer.

When considering the anisotropy of the data, a distinction is made by the program Staraniso for the unmeasured reflections between observable and unobservable, i.e., reflections that fall within the anisotropic cut-off surface and would therefore have been expected to be observed, and those that fall outside of that cut-off surface and should therefore not be included for structure refinement or map calculations. Using the program Buster for reciprocal-space structure-refinement, it was possible to avoid all unobserved reflections having their structure

factors replaced by DFc, which would have resulted in unrealistic, model-biased electrostatic potential maps. These limitations notwithstanding, the gain in resolution afforded by SerialED is substantial, suggesting that if the crystals had not been subject to a preferred orientation, a complete, isotropic dataset extending to at least 1.8 Å resolution would have been achievable (Fig. 5).

Using the SFX model as the basis for comparison we interrogated all three models with an aim to provide insight into the effects on Cry11Aa of beam damage (3DED vs. SerialED), vitrification to 80 K (SerialED vs. SFX) and their confluence (3DED vs. SFX). First, we used Difference (Cα)-Distance Matrices (DDMs)[62] (Fig. 6a). In the DDM computed between the 3DED and SerialED models, it can be seen clearly that electron damage is manifest as an expansion of the protein, mostly visible in domains I and III (Fig. 6a), and in the distance between domain I and the rest of the structure. At variance, the DDM computed between the 3DED and SFX models shows a global compaction of the protein, consistent with the ~3.5% reduction observed in unit cell volume and attributed to the effect of vitrification to 100 K. It is worth noting that domain I, which is aligned with the b-axis showing the greatest sensitivity to temperature, is the least compacted of the three domains. When comparing models derived from the SerialED and SFX data, we see a situation in between the two described above, i.e., a compaction of the protein is seen that can be attributed to vitrification, but which does not affect the whole protein. Domains I and III show reduced compaction compared to domain II, and the relative position of domain I with respect to the rest of the protein is unchanged compared to the room-temperature SFX structure. One possible explanation is that following continuous exposure of the crystals to the electron beam in 3DED, the temperature rises locally, both enabling the domain re-organization visible in the 3DED-SerialED DDM and reversing the compaction of the protein on vitrification to 80 K; indeed, the reduction in unit cell volume is only 0.5 % when the SFX and 3DED dataset are compared. Alternatively, this could be due to differences in the vitrification procedure translating to different crystal/unit-cell compaction patterns. To further investigate the structural differences between the 3DED, SerialED and SFX models, we used Xtrapol8[63], a software that computes Fourier difference maps between two datasets, providing insights into the structural regions which are prone to structural rearrangements, as well as generates extrapolated structure factors to identify and model low-occupancy intermediate-states which might be present between these two datasets (Fig 6b). All three Fourier difference maps (namely, $Fobs^{3DED}$-$Fobs^{SerialED}$, $Fobs^{3DED}$-$Fobs^{SFX}$, $Fobs^{SerialED}$-$Fobs^{SFX}$) contained strong features. The observations of more negative peaks than positive ones suggest increased disorder in the 3DED model compared to the SerialED and SFX ones (due to damage and / or vitrification), but as well in the SerialED model compared to that from SFX (presumably due to vitrification only). Models derived from refinement against extrapolated structure amplitudes show dramatically reduced global deviation from their

reference state, from which we deduce structure factor extrapolation is a convenient procedure to examine the local effects of vitrification and/or radiation damage decoupled from global changes (inter-domain movements) arising e.g. from unit cell compaction. Taken together, the data illustrate the advantages of using SerialED instead of 3DED, as the reduction in cumulative radiation damage not only directly translates to higher resolution data but also to reduced global changes in the protein structure. Likewise, there is an argument for a potential superiority of SerialED over SFX, given the attained resolution by the two techniques. The caveat is that SerialED requires vitrification, which we show induces global structural changes in the crystalline protein.

SerialED of other *Bt* crystalline-toxins

Given the improvement in resolution observed with Cry11Aa, we have tested the limits of our approach by collecting SerialED data from several other *Bt* crystalline-toxins. CryoEM grids were prepared for three types of crystalline-toxins, viz. *Bt israelensis* Cyt1Aa, *Bt alesti* Cry1Ae and C11AB, a fusion of Cry11Aa with the 77-residue C-terminal extension of Cry11Ba (Tetreau et al., 2022, Nat Comm). A model currently exists of Cyt1Aa, obtained from SFX data collected at 1.8 Å resolution[14]. A model for Cry1Ae has yet to be obtained. The crystals of the C11AB fusion were previously analysed by SFX but only diffracted to 6 Å at XFEL[18] either due to their small size, making them too challenging even for SFX, or to intrinsic disorder owing to suboptimal packing of the fusion.

In our studies purified crystals were first screened by SEM and TEM to assess their suitability for ED (Supplementary Fig. 4, Supplementary Fig. 5a-c). In all cases a lattice could be observed by TEM, although the Cyt1Aa and Cry1Ae crystals appeared to be quite thick due to their bipyramidal morphology. In contrast the C11AB crystals appeared amorphous in the SEM (Supplementary Fig. 5d) but were shown to be small crystalline fragments when viewed by TEM, each with a single lattice visible (Supplementary Fig. 5c). SerialED datasets were collected from each of the three crystal preparations using a ~80 nm parallel beam, which in some cases impinged as few as 750-unit cells. Cry1Ae and Cyt1A produced diffraction patterns extending to 2.3 Å, reaching the resolution-limit of the detector in our experimental setup (Supplementary Fig. 5d-f), while diffraction to 3.0 Å was observed for C11AB. Whilst Cyt1A crystals did not diffract to a resolution comparable to the one achieved with SFX (1.8 Å), presumably due to sub-optimal vitrification and greater thickness of the crystals, diffraction of C11AB crystals showed significant improvement, which we propose to result from the smaller size of these engineered crystals falling into the ideal size range for ED (Supplementary Fig. 5c). These experiments demonstrate the potential of SerialED to extract

data at meaningful resolutions from crystals that cannot be exploited by any other diffraction technique otherwise.

Discussion (1075 words)

The results reported here illustrate the potential of electron diffraction methods for solving challenging nanocrystalline protein structures. We have focused on naturally-occurring nanocrystals of 27-133 kDa pesticidal proteins featuring ~75,000 – 1,000,000 unit cells. In the natural context, these crystals are produced within the confines of *Bt* cells during their starvation-induced sporulation, with the aim of being ingested by, killing, colonising and then germinating on insect or nematode larvae. Owing to the limited number of unit cells, these crystals pose a challenge for conventional crystallography, which explains why until this work, atomic-resolution structure determination has been limited to scarce beam times at XFEL sources. We show that for crystals of Cry11Aa, featuring 75,000 unit cells on average, electron diffraction data compares favourably with that obtained by SFX, with 3DED achieving a similar resolution (2.9 vs 2.6 Å). Energy-filtering of the 3DED data was essential in this case as the comparatively large amount of solvent surrounding these small crystals produced a significant inelastic background, which furthermore varied along the tilt axis due to changes in the apparent ice-thickness. The improvement in 3DED data quality and resolution observed upon applying energy-filtering is consistent with previous observations on other protein crystals[54,64]. For 3DED, radiation damage remains a persistent problem, requiring the merging of data from many different crystals (here 39) and limiting the achievable resolution. This led us to investigate the potential of SerialED, where a unique high-dose pattern is collected for each of the thousands of irradiated crystals, to maximise the resolution of the structural data. SerialED allowed diffraction data to be collected at resolutions beyond what was possible by 3DED and even surpassed results obtained by SFX (2.2 or 1.92 Å, depending on whether an isotropic or anisotropic cut-off is applied). Our results demonstrate that by using 3DED in conjunction with SerialED, it is possible to overcome the limitations of both techniques. Our energy-filtered 3DED data were of sufficient quality to naively assign the correct unit cell parameters from the measured data, which remains challenging for SerialED[65]. Here the space group assignment remained ambiguous between I222 (correct) and the three alternative lower-symmetry C2 space-groups. With the confident assignment of lattice symmetry based on 3DED, it was possible to collect SerialED data of the same crystals and strongly mitigate, if not eliminate, electron damage to the biological structure.

Our preliminary analysis of 3 other naturally-crystalline proteins from *Bt*, including a synthetic fusion of Cry11Aa with the C-terminal tail of Cry11Ba (C11AB) that had diffracted poorly at the XFEL[18], further highlights the potential of SerialED to overcome crystal size and quality limits and be applicable to *Bt* derived as well as morphologically similar crystals. Indeed, we have studied two crystalline proteins where ED achieved a superior resolution compared to SFX. Nevertheless, the highest resolution for Cyt1Aa was still achieved by SFX at XFEL, consistent

with results from other studies[66,67]. There can be several reasons for this including the higher intrinsic sensitivity of some proteins to radiation damage by the electron beam[43] and the morphology of the crystals. In particular, the bipyramidal shape of Cyt1A (and Cry1Ae) was not optimal for ED as the centre of the crystal was too thick for electrons to penetrate. This is particularly problematic for crystals with large unit cell dimensions as it has been demonstrated that a minimum thickness of 5-unit cells is required to acquire sufficient data for structure determination by 3DED[68]. Indeed, among the structures that have currently been solved by ED in the PDB we note that there seems to be a link between unit cell volume and the resolution achieved, likely due to the finite thickness accessible to electrons (Supplementary. Fig. 6). Therefore there is case to be made that electron crystallography could benefit from the use of TEM and 4DSTEM at higher electron energies than those used in this and related studies. Irrespectively, our data show that atomic-resolution structural-insights into *Bt* crystalline-toxins are within reach of ED techniques.

Of the hundreds of such toxins, only a handful have been structurally characterised experimentally. Resistance to *Bt* proteins is increasing and being able to experimentally characterise new, functional mutants is critically important. The workflow presented here positions ED as a vital tool in improving our understanding of the native packing of these pesticidal proteins within the bacterial cell. From a broader perspective, ED techniques could also be relevant for similarly sized naturally-occurring crystals produced by other biological systems. Indeed, there is a growing body of work demonstrating the advantages of electrons for studying molecular nanocrystals grown within a cellular context[69,70]. The previously mentioned limitation on sample thickness means electron diffraction cannot be considered a general technique for structure determination of all protein nanocrystals grown *in vivo*. Indeed, a current requirement to applying ED techniques is that crystals remain stable in water or another vitrification compatible buffer after extraction from cells, as probing their structure *in situ* would be challenged by the augmented thickness of scattering material. In this context, related electron-microscopy methods such as cryoFIB-SEM are required to enable exposure of the crystals (or fragments thereof) from the cells[71,72]. The work of Yang et al is particularly relevant as the system studied in this paper, eosinophilic major basic protein (eMBP), was approached by SFX, but structural insights were limited to demonstrating that the packing of individual protein chains differs in the natural nanocrystals and those obtained by recrystallising the protein i*n vitro*[73]. By contrast ED techniques combined with cryoFIB-SEM, were able to interrogate the *in-situ* structure of eMBP and assess structural differences arising from eosinophil activation[70].

In conclusion, our work demonstrates that ED is a valuable addition to the protein nanocrystallography toolbox, particularly for structure determination of protein nanocrystals

grown *in cellulo*. Our results suggest that recent (and future) advances in detector technology[50,74,75] and sample preparation[76–78] will broaden the applicability of these techniques. More specifically, 3DED can provide a robust and accessible platform for protein nanocrystallography using conventional electron microscopes and established crystallographic software. SerialED, in contrast, requires more specialised instruments but has the potential to produce data of superior quality. Furthermore, we expect incorporating energy-filtering into the SerialED workflow will provide similar benefits to those observed in 3DED, such that data quality may be further improved. As new tools and protocols emerge for reliably producing protein nanocrystals we expect a growth in the application of ED for protein structure determination, similar to the boom that has been observed for chemical crystallography[79].

Materials and Methods

Crystal expression and purification

Cry11Aa crystals were produced and purified as previously described (Tetreau et al, 2022, Nat Comm). Briefly, acrystalliferous (plasmid-curated) cells of *Bacillus thuringiensis israelensis* (strain 4Q7; The Bacillus Genetic Stock Center (BGSC), Columbus, USA) were transformed by electroporation with the pWF53 plasmid[80] featuring : (i) the *cry11aa* gene under control of its natural promoter; (ii) the *P20* gene under control of the Cry1Ac promoter; (iii) replication origins suited for amplification in *E. coli* and expression in *Bt*, respectively; and (iv) resistance cassettes for erythromycin (*Bt* selection) and ampicillin (*E. coli* selection). Transformed cells were deposited on LB agar medium supplemented with erythromycin (25 µg/mL), and after two days, a colony was swept to inoculate an LB pre-culture, also supplemented with 25 µg/mL erythromycin. For the production phase, precultures were spread on T3 sporulation medium (Tryptose 2 g L-1, Tryptone 3 g L-1, yeast extract 1.5 g L-1, Na2HPO4 1.4 g.L-1, NaH2PO4 1.2 g.L-1, MnSO4, MgSO4, and ionic solution 1 mL per 1 L (in 1 L of H2O: 6.82 g ZnCl2, 101.66 g MgCl2.6H2O, 1.98 g MnCl2.4H2O, 29.4 g CaCl2.2H2O, 13.52 g FeCl3.6H2O, 967 µL 10 M HCl)) containing 25 µg/mL erythromycin., and after incubation for 4 days at 30°C, spore and crystal were recovered using cell scrapers, pooled and resuspended in ultra-pure water. Cells were lysed by several cycles of sonication (1 sec excitation pulse at 0.5 Hz during 1 minute) at 100 W, centrifuged at 4,000 *g* for 45 minutes to remove cell debris and medium, and then centrifuged again at 10,000 g to pellet crystals and spores. The pellet was resuspended in water and the crystals were isolated from the spores and remaining cell debris by ultracentrifugation (23,000 × g, 4°C, 17 h) on a discontinuous sucrose gradient (67-72-79%). After ultracentrifugation, the crystals were recovered at the 67-72% interface, and thereafter washed by several cycles of centrifugation/resuspension in ultra-pure water to eliminate sucrose. The purity and integrity of the crystals was assessed by SDS-PAGE on 12% gels and by scanning electron microscopy (Ultra-55 Zeiss, Zeiss, Germany) on the nano-characterization platform (IRIG-CEA, Grenoble, France), respectively. Crystals were stored in ultra-pure water and at 4°C before use.

Cyt1Aa and C11AB crystals were produced and purified as previously described[14,18]. Transformation, expression and crystal-purification were performed as described above for Cry11Aa.

Crystal visualisation using scanning electron microscopy (SEM)

Purified crystals of Cry11Aa, Cyt1Aa, Cry1Ae and C11AB were imaged using a Zeiss Ultra 55 scanning electron microscope at the nanocharacterization platform in the Institut de Recherche Interdisciplinaire de Grenoble (IRIG). Samples were coated with a 2 nm thick layer of gold using a Compact Coating Unit-010 sputtering unit (Safematic®) prior to imaging. Images were recorded at 5-20 kV acceleration voltage by collecting secondary electrons using an Everhart-Thornley-Detector (ETD detector) in high-vacuum mode.

CryoEM grid preparation

For 3DED experiments a slurry of purified Cry11Aa crystals was first diluted 1000-fold in 10% glycerol and 2 µl of diluted crystal suspension were applied to the carbon side of a freshly glow discharged (60 s 20 mA, Pelco Easyglow) holey carbon grid (300 mesh Cu (emResolutions)). A solution of 2 µl of 10% glycerol was then applied to the opposite side of the grid and excess solution was removed by single side back blotting in a Leica EM GP2 (7s, 85% humidity, 4 C) before plunge freezing into liquid ethane.

For SerialED experiments of Cry11Aa, a slurry of crystals was prepared as for the 3DED experiment. A volume of 3.5 µl of suspension was applied to the carbon side of a freshly glow discharged hole-array grid (Quanitfoil R1.2/1.3). Two-sided blotting was applied in a FEI Mark IV (FEI Company), before plunge freezing into liquid ethane.

For SerialED experiments of the other *Bt* crystals, crystalline slurries were resuspended in 10% glycerol and 3 µl of these suspensions were applied directly to freshly glow discharged (60s 20 mA, Quorum GloQube Plus) Quantifoil grids (1.2/1.3 400 mesh Cu). Excess solution was removed by double sided blotting in a Vitrobot Mark IV (Thermo Fisher Scientific) using parameters optimised for each crystal type (generally blot time of 10 - 15s, blot force of 10 - 15, 20s wait time, 1s drain time, 80% humidity, 20 c) before plunge freezing into liquid ethane.

3DED data collection

Frozen hydrated EM grids were transferred into a JEOL cryoARM300 operating at 200 kV for data collection. The A2 gun lens voltage was reduced from 3.33 kv to 3.13 kv to reduce the incident fluence at the sample. A camera length was selected such that the top edge of the K2 detector corresponded to 2 Å resolution using a gold cross grating as a calibration standard. Diffraction quality crystals were identified in an over-focussed diffraction mode by maximising the excitation of the third condenser lens. Crystals were manually brought to the goniometer eucentric height and the excitation of third condenser lens was then reduced to form a parallel

beam with a flux of 0.015 $e^-/Å^2/s^{-1}$ for 3DED data collection. Diffraction movies were collected semi-automatically using SerialEM[81] to synchronise stage movement with the camera operation. Crystals were isolated using a 50 µm selected area aperture (0.8 µm field of view at the sample plane) and each crystal was rotated over a 30-degree wedge with a rotation speed of 0.1 degrees per second giving a total fluence of 4.5 $e^-/Å^2$. Data was recorded on a K2 DE detector in counting mode below an omega filter with a frame time of 1s. Energy filtered data was collected with a slit width of 30 ev or the slits were completely removed for unfiltered data. Due to the low fluence it was possible to record data without a beam stop. A total of 47 zero-loss filtered and 27 unfiltered datasets were collected.

Data reduction, phasing and model building for 3DED

Raw data frames in LZW compressed tiff format were pre-processed using a custom python script that performed drift correction, diffraction pattern centring, hot pixel removal, gain correction and binning before outputting data in MRC format. Frames were binned by 2 in the x and y dimensions and 10 in the temporal dimension to give 30 frame stacks where each frame represents a 1-degree wedge of data. Data reduction (spot, finding, indexing, refinement, integration and scaling) was performed in DIALS[82,83] using the first 20 frames to reduce the impact of radiation damage. A single dataset with the highest quality diffraction was analysed first and the space group was determined to be I222 by the routine dials.refine_bravais_setting. This space group was then used as a constraint during automated processing of all 47 datasets. The xia2.multiplex program[84] was used to assess the best movies to merge and the final resolution cut off of 2.85 Å using a cluster containing 39 of the 47 datasets. Phasing was performed by molecular replacement using a model generated by AlphaFold3 from the sequence of Cry11Aa. Low confidence residues were trimmed automatically in Phenix[85] and a single solution was found in Phaser[86] with space group I222, an LLG of 1122.5 and a TFZ of 32.0. Refinement of this model was performed by alternating between automated refinement in Phenix, using electron scattering factors, and manual adjustments performed in Coot[87] to produce a final model with an rWork/rFree of 0.1713/0.2386.

Filtered vs. Unfiltered background comparison

Datasets containing the same angular wedge with the energy selecting slit either inserted or fully open were selected and a 5-degree angular wedge was chosen to sum such that the Bragg peaks visible in the image corresponded to a complete sampling of Bragg intensity. Line profiles were drawn in Fiji and then analysed in python. For the data with the slit fully open an

asymmetric loss function was fit to the 1D profile to estimate a smooth background whilst penalising fits to the higher intensity peaks. This background was then subtracted from the 1D profile to compare the two datasets at the same background level. This process was not necessary for the energy filtered data.

SerialED data collection for Cry11Aa

SerialED data from Cry11Aa were collected using a Philips Tecnai F20 field-emission S/TEM operating at 200 kV, equipped with a custom-built hybrid pixel detector (DESY detector group) based on a Medipix3 chip (1556x516 pixels), synchronized to a custom-built beam scanning system (based on a National Instruments PCI-6251 DAQ board) allowing for arbitrary patterns of fast beam movement and scanning. The sample grids prepared as described above were transferred into the S/TEM using a Gatan Model 626 cryo-transfer holder. Detailed Instrument setup, sample screening and data collection are described in detail in[45]. Mapping images over a field of view of 18x18 µm² were collected from each region ADF-STEM mode at a total fluence of <0.1 e^-/Å². Using image segmentation, positions of nanocrystals are automatically identified for SerialED data collection. For the ensuing data collection step, the beam was defocused using the C2 condenser to give a parallel condition (~0.1 mrad) with a diameter of ~110 nm, defined by a 5 µm condenser aperture. By setting the gun lens of the field-emission gun to its lowest excitation and the C1 condenser lens to Spotsize 6, a beam current of 14 pA was achieved with the 5 µm condenser aperture, yielding a flux density of 92 e^-/A²/s^{-1} on the crystals. Data was collected in a dose-fractionated mode by setting the frame time of the detector to 2 ms with 20 frames collected from each crystal, corresponding to a total fluence (dose) of 0.18 e^-/A² per movie frame and 3.7 e^-/A² for the entire movie. During processing, it was found that optimal data quality (gauged by merging metrics and spot intensities) was achieved by summing up all frames for each crystal in the final data processing, i.e., the full fluence of 3.7 e^-/A² per crystal was used in the final dataset. The projection system of the S/TEM was set to an effective camera length of 3062 mm on the detector, corresponding to a maximum diffraction resolution of 1.8 Å near the long edge of the detector. The camera length and a residual elliptical distortion of ~2% was calibrated using diffraction ring patterns from a polycrystalline thallous chloride standard (Ted Pella).

Data reduction, phasing and model building for SerialED

Data were processed using diffracTEM[65] and CrystFEL (v. 0.10.0+9438abb0)[59], with PinkIndexer serving as the indexing algorithm[60]. Of 14620 collected images, 12625 could be

indexed (*indexamajig* program) and were retained for Monte-Carlo merging (*process_hkl* program). Only reflections measured five times, or more were included in the merge. Post-refinement of the data (*partialator* program*)* was attempted with both the 'xsphere' and the 'unity' models[88,89], and gave good results based on figure of merits (Supplementary Fig. 3). However, completeness and multiplicity were negatively impacted, which resulted in electron potential maps of lesser quality, notwithstanding whether or not Staraniso[61] was used in a second step to find and apply an anisotropic diffraction cutoff for refinement and map calculations. Likewise, Monte Carlo averaging using the 'second-pass' (scaling) option in CrystFEL *process_hkl* yielded data of worse quality, as did the inclusion of polarization corrections or the treatment of Friedel pairs as separate reflections. Hence, reported results are derived from the structure factors amplitudes estimates obtained by simple MonteCarlo averaging, with Friedel law considered true. These issues are likely due to our limited amount of data, which translates to low completeness and multiplicity and therefore to high uncertainty in the estimation of structure factor amplitude. Furthermore, we conjecture that due to the homogeneous size and shape of the crystals, a simple averaging of intensities collected from each one is justified even for a comparatively small number of crystals, as opposed to merging data from more diverse crystals where more involved refinements are beneficial.

After estimation of the anisotropy diffraction cutoff using Staraniso, phasing of the SerialED data was achieved by rigid-body refinement using the program Buster with the "-RB" command line argument[90], after which the structure was refined by iterative cycles of reciprocal space refinement in Buster (with "-M ElectronDiffraction -nsmall 200 -nbig 5 -r 0.005 -w 1 -rpolicy tight -WAT" as command line arguments) and real-space refinement in Coot[87] (, selecting as map coefficients for the model real-space fitting the Buster-specific 2FOFCWT_aniso_fill and PH2FOFCWT_aniso_fill. Analysis of structural differences was carried out using Xtrapol8[63] and custom-written scripts. Figures were produced with PyMOL and ChimeraX[91].

SerialED data collection for other *Bt* crystals

Samples were loaded into a double corrected JEOL GrandARM2 TEM operating in nanobeam diffraction (NBD) mode using a cryo transfer holder (Fischione, Model 2550). Coma and twofold astigmatism were adjusted manually using the ronchigram. With this optical geometry it was possible to form a ~ 80 nm diameter parallel probe using a 10 µm condenser aperture by adjusting the excitation of the second condenser lens to give Kohler illumination. A simple script was implemented in pyJem to rapidly switch between the convergent STEM illumination and the parallel SerialED illumination. The measured probe current was 22 pA giving a fluence of 0.35 e-/Å^2 per frame assuming a 2 ms dwell time. The camera length was set at 800 mm

which corresponds to a true camera length of 1346 mm based on diffraction from the gold cross-grating. Low magnification STEM (2500x magnification with a 512 by 512 raster) was used to identify grid squares with suitable sample distribution and the stage positions were recorded.

Data collection was performed using a set of scripts implemented in python and Julia to control the movement of the STEM scan coils (Quantum Detectors Scan Engine) and synchronise this with data acquisition on a MerlinEM 4R detector (Quantum Detectors). Data collection proceeded as follows. Firstly, the microscope was set to STEM mode and search STEM scans were recorded at 20kx with an 80 nm step size (i.e. a 128 X 128 scan) and a 20 µs dwell time, giving a fluence of 0.0025 $e^-/Å^2$ per scan. Crystal coordinates were then computationally segmented from the STEM image and the microscope switched to a SerialED mode. The beam was then moved to the segmented coordinates as an arbitrary scan to collect data. Data were recorded as 2ms x 10 frame stacks such that the total fluence at each coordinate is 3.5 e-/Å^2. 'Good' hits for further processing were determined based on the amount of signal beyond a low spatial frequency cut-off, to avoid the high signal at the primary beam. A radial background was subtracted to aid with Bragg peak visualisation.

Data availability

Coordinates and structure factors for Cry11Aa determined by 3DED and SerialED at 2.2Å and 1.9Å resolution cutoffs have been deposited in the RCSB Protein Data Bank under accession codes 9RML, 9RMP and 9RMN respectively. 3DED datasets and SerialED data streams, alongside the microscope control and data analysis scripts, have been placed in a Zenodo repository, entry 15691475.

Acknowledgments

We thank Brian Federici for kindly providing the pWF53 & pWF45 plasmid used for production of Cry11Aa and Cyt1Aa crystals, respectively. We thank Martin Weik, Didier Lereclus and Michel Gohar for continuous support. We also warmly thank Elke De Zitter for implementation of the use of electron scattering factors in Xtrapol8. MGJ thanks David Waterman for assistance with processing ED data in DIALS. IBS acknowledges integration into the Interdisciplinary Research Institute of Grenoble (IRIG, CEA). This work was supported by the Agence Nationale de la Recherche (grants ANR-17-CE11-0018-01, ANR-20-CE11-0019-02 and ANR-22-CE11-0016 to J.-P.C.). Platform access was supported by FRISBI (ANR-10-INBS-05-02) and GRAL, a project of the University Grenoble Alpes graduate school (Ecoles Universitaires de Recherche) CBH-EUR-GS (ANR-17-EURE-0003). RJDM's work is Supported by the Natural Sciences and Engineering Research Council of Canada. MGJ, JSK

and AIK acknowledge funding from the Engineering and Physical Sciences Research Council to the Rosalind Franklin Institute. QD was funded by the 80PRIME PhD Program of the CNRS and received support from MITACS and the UGA through a Globalink Research Award.

Notes. RJDM is one of the inventors of a patent on Serial NED.

Tables

Table 1 Data collection and refinement statistics (molecular replacement)

	Cry11Aa, ef3DED	Cry11Aa, SerialED - isotropic cutoff	Cry11Aa, SerialED - anisotropic cutoff	Cry11Aa, SFX
PDB accession code				7QX4[c]
Data collection				
Wavelength (Å)	0.025	0.025	0.025	1.27
Space group	I222	I222	I222	I222
Cell dimensions				
a, *b*, *c* (Å)	58.1, 153.1, 171.7	56.9, 155.2, 168.0	56.9, 155.2, 168.0	57.6, 155.7, 171.1
α, β, γ (°)	90, 90, 90	90, 90, 90	90, 90, 90	90, 90, 90
Probe size (µm)	0.8	0.1	0.1	5
Number of crystals	39	14620	14620	48652
Number of indexed patterns	1410	12625	12625	50613
Number of merged images	1170 [b]	12625[b]	12625[b]	48652[b]
Resolution (Å) [a]	114.25-2.85 (2.90-2.85)	43.5-2.23 (2.28-2.23)	43.5-1.96 (1.97-1.96)	33.55-2.60 (2.66-2.60)
Number of observations	739054 (26334)	4539099 (71901)	4969184 (57296)	8253629 (365007)
Number of unique reflections	15107 (731)	25369 (1106)	33501 (1390)	24198 (1583)
I/σI [a]	10.0 (1.7)	4.38 (0.67)	3.42 (0.21)	9.50 (1.16)
Rsplit (%) [a]	n.a.	0.216 (1.612)	0.250 (4.479)	0.107 (0.954)
Rpim	0.084 (0.305)	n.a.	n.a.	n.a.
Rmerge	0.574 (1.830)	n.a.	n.a.	n.a.
$CC_{1/2}$ [a]	0.980 (0.214)	0.967 (0.242)	0.967 (0.04)	0.993 (0.377)
Completeness (%)[a]	82.17 (79.80)	66.42 (44.03)	56.87 (36.19)	99.9 (100.0)
Multiplicity [a]	48.9 (36.0)	178.9 (65.0)	148.3 (41.2)	341.09 (230.5)
Diffraction limit along a*	2.6	2.3	2.3	2.5
Diffraction limit along b*	3.5	1.8	1.8	2.7
Diffraction limit along c*	2.6	2.1	2.1	2.5
Refinement				
Resolution (Å) [a]	2.85	2.23	1.8	2.6
Number of reflections [a]	16099	17339 (1231)	17339 (1231)	24196
R_{work} / R_{free} [a]	0.174 / 0.240	0.231 (0.459) / 0.295 (0.547)	0.231 (0.459) / 0.295 (0.547)	0.172 / 0.241
Number of atoms				
Protein	5044	5025	5025	5080
Water	108	177	177	261
B-factors ($Å^2$)				
Protein	38.4	32.6	32.6	50.91
Water	23.2	52.3	52.3	46.17
R.m.s. deviations				
Bond lengths (Å)	0.004	0.007	0.007	0.004
Bond angles (°)	0.649	1.083	1.083	0.633

[a] Values in parentheses are for highest-resolution shell. [b] The number of merged images corresponds to number of crystals for serial data and number of frames for 3DED data. [c] Published in previous work (Tetreau et al., 2022, Nat Comm) and used to solve the SerialED structure by molecular replacement.

Table 2 Data collection statistics for 3DED data without Energy-filtering

	Cry11Aa, 3DED - filter out	Cry11Aa, 3DED - filter out, high-res cutoff
Data collection		
Wavelength (Å)	0.025	0.025
Space group	I222	I222
Cell dimensions		
a, *b*, *c* (Å)	58.0, 153.1, 171.6	58.0, 155.5, 171.8
α, β, γ (°)	90, 90, 90	90, 90, 90
Probe size (µm)	0.8	0.8
Number of crystals	27	27
Number of indexed patterns	810	810
Number of merged images	450	330
Resolution (Å) [a]	85.81-3.73 (3.79-3.73)	85.91-2.99 (3.05-2.99)
Number of observations	123801 (6442)	141536 (2803)
Number of unique reflections	7255 (364)	10362 (261)
I/σI [a]	6.8 (3.7)	5.2 (2.0)
Rpim	0.123 (0.209)	0.146 (0.320)
Rmerge	0.481 (0.814)	0.544 (1.013)
$CC_{1/2}$ [a]	0.743 (0.373)	0.940 (0.388)
Completeness (%)[a]	87.10 (87.90)	61.77 (34.51)
Multiplicity [a]	17.1 (17.7)	13.7 (10.7)

[a] Values in parentheses are for highest-resolution shell.

Figures

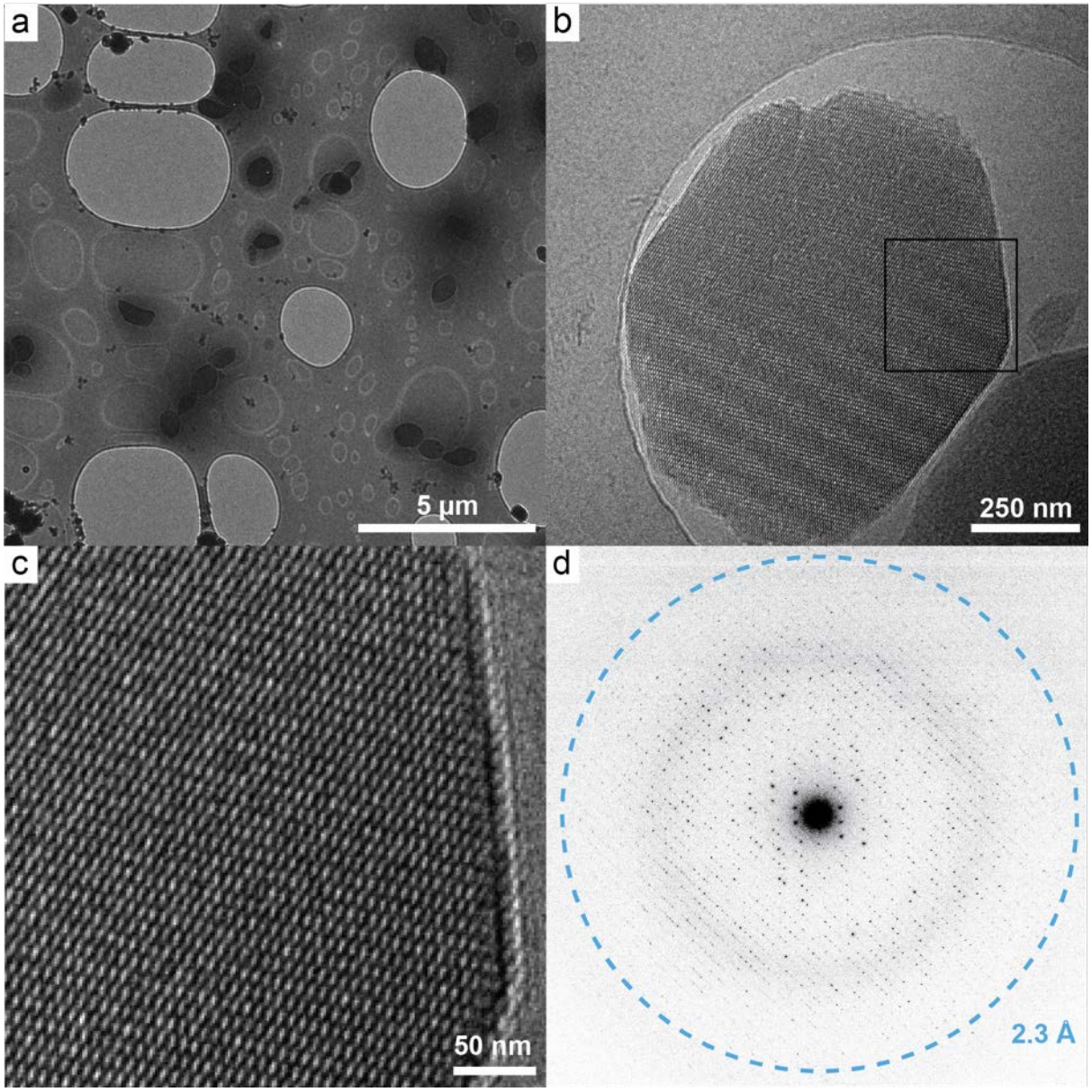

Fig. 1. Energy filtered Electron Diffraction of Cry11Aa nanocrystals. a) Overview of frozen-hydrated Cry11Aa nanocrystals on a holey carbon EM grid. b) Higher magnification EFTEM image of an individual crystal showing sharp faceted edges. c) Zoom in of highlighted region in (b) showing clear contrast for individual unit cells. d) Selected area energy filtered ED pattern recorded on a K2 detector in counting mode showing diffraction extending beyond 2.3 Å resolution.

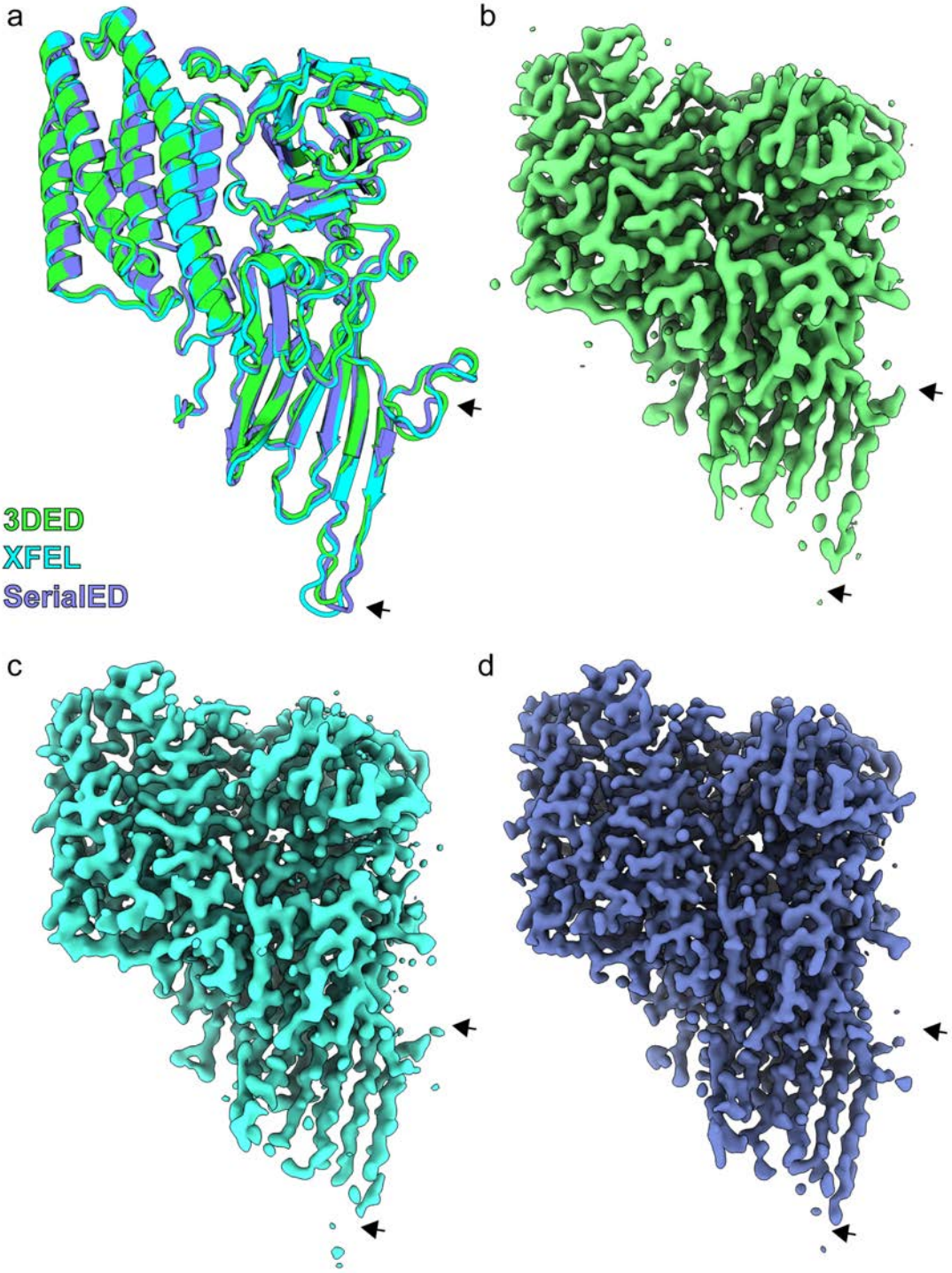

Fig. 2. Cry11Aa structures solved by different diffraction methods have the same overall topology and density. a) Alignment of all 3 structures of Cry11Aa in cartoon representation showing good agreement in the overall structure. b) Coulomb potential map calculated from the 3DED data. c) Electron density map calculated from the XFEL data. d) Coulomb potential map calculated from the SerialED data. All maps are thresholded at 2 σ. Black arrows indicate loop and β-turn regions where the majority of the deviations between the structures occur. The position of the black arrows indicative of weaker density is conserved across all four panels.

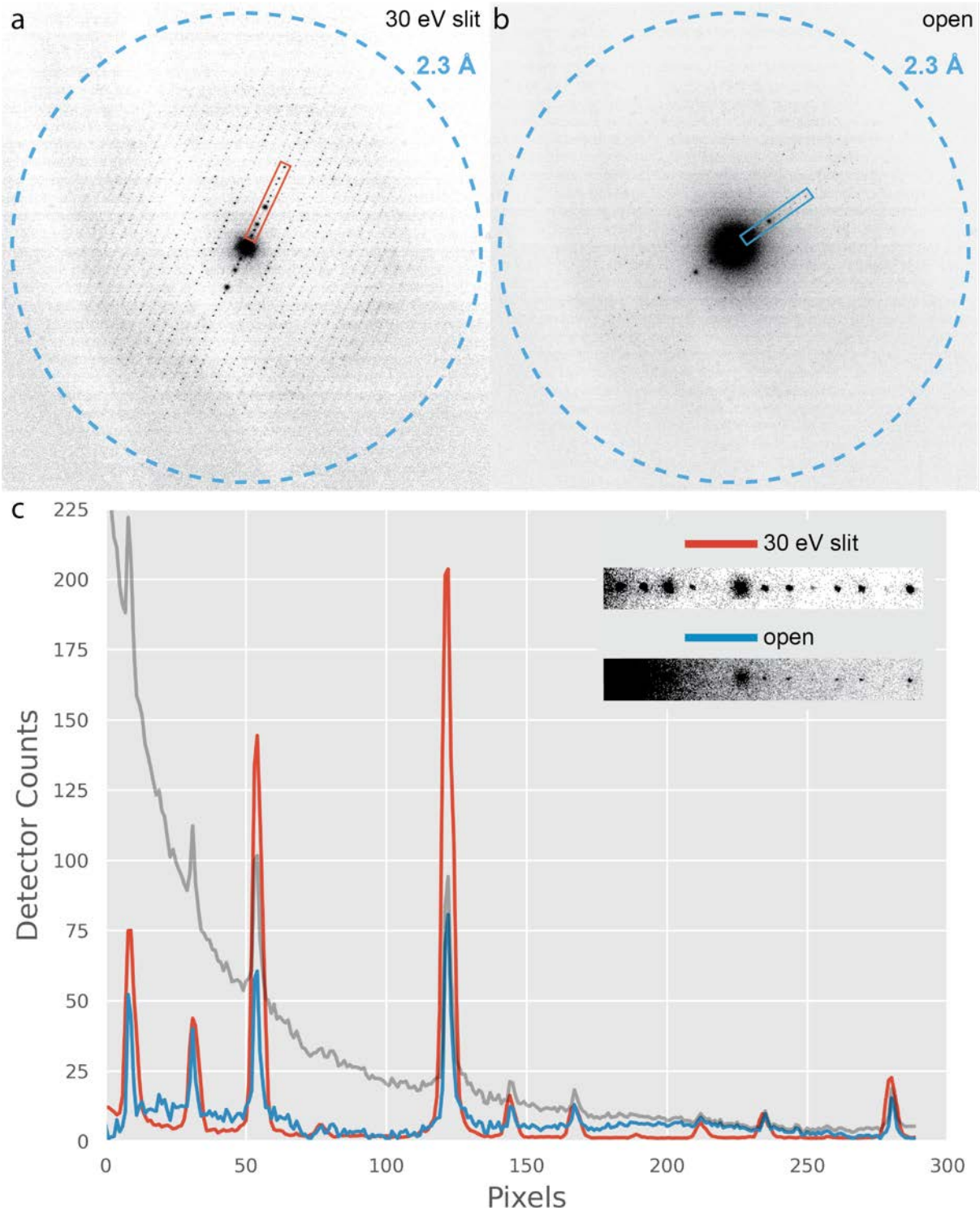

Fig. 3. Background subtraction is not sufficient to improve the SNR of unfiltered electron-counted 3DED data. a) A five-degree wedge extracted from a 3DED dataset of Cry11Aa with a 30 eV energy slit inserted. b) The same five-degree wedge of data from a different Cry11Aa nanocrystal with the energy slits completely removed. c) Line profile of the peaks indicated in A and B. A background was fit to the unfiltered data and subtracted; the 30 eV slit data is the raw data with no subtraction. The light grey plot is the raw unfiltered data prior to background subtraction.

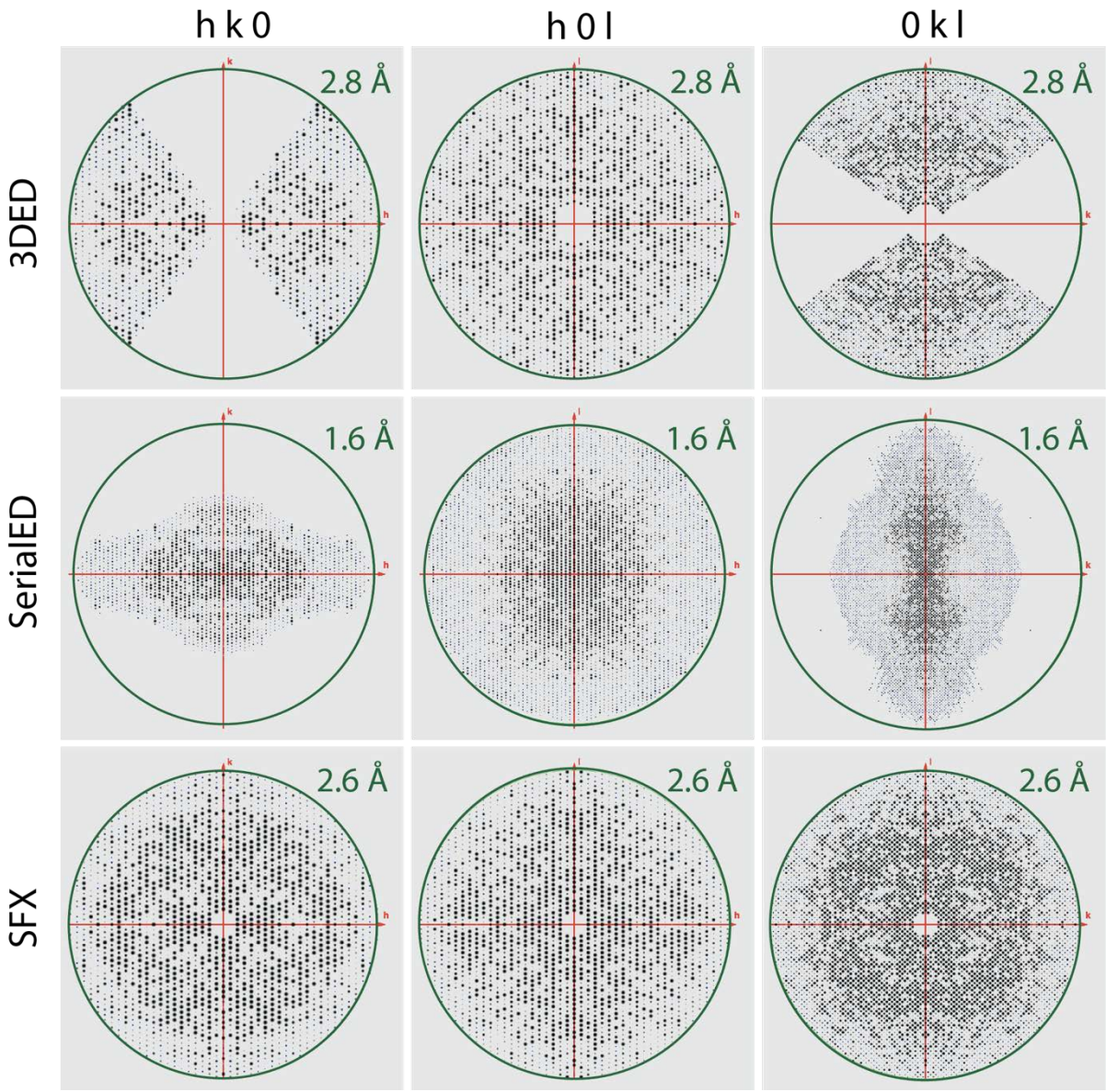

Fig. 4: Resolution and completeness of data vary depending on the nanocrystallographic structure determination approach. Integrated reflections are shown for the hk0, h0l and 0kl zones in each of the three datasets. The 3DED data extend to 2.8 Å after merging, despite first frames generally extending to 2 Å and beyond. A large wedge of reflections is missing due to the limited rotation range of the goniometer installed in the microscope. The SerialED data extend to 1.6 Å, but only in one direction, which can be ascribed to preferential orientation of the Cry11Aa crystals on the grid and be dealt with by application of an anisotropic diffraction cutoff. The SFX data extend to 2.6 Å resolution but are fully isotropic.

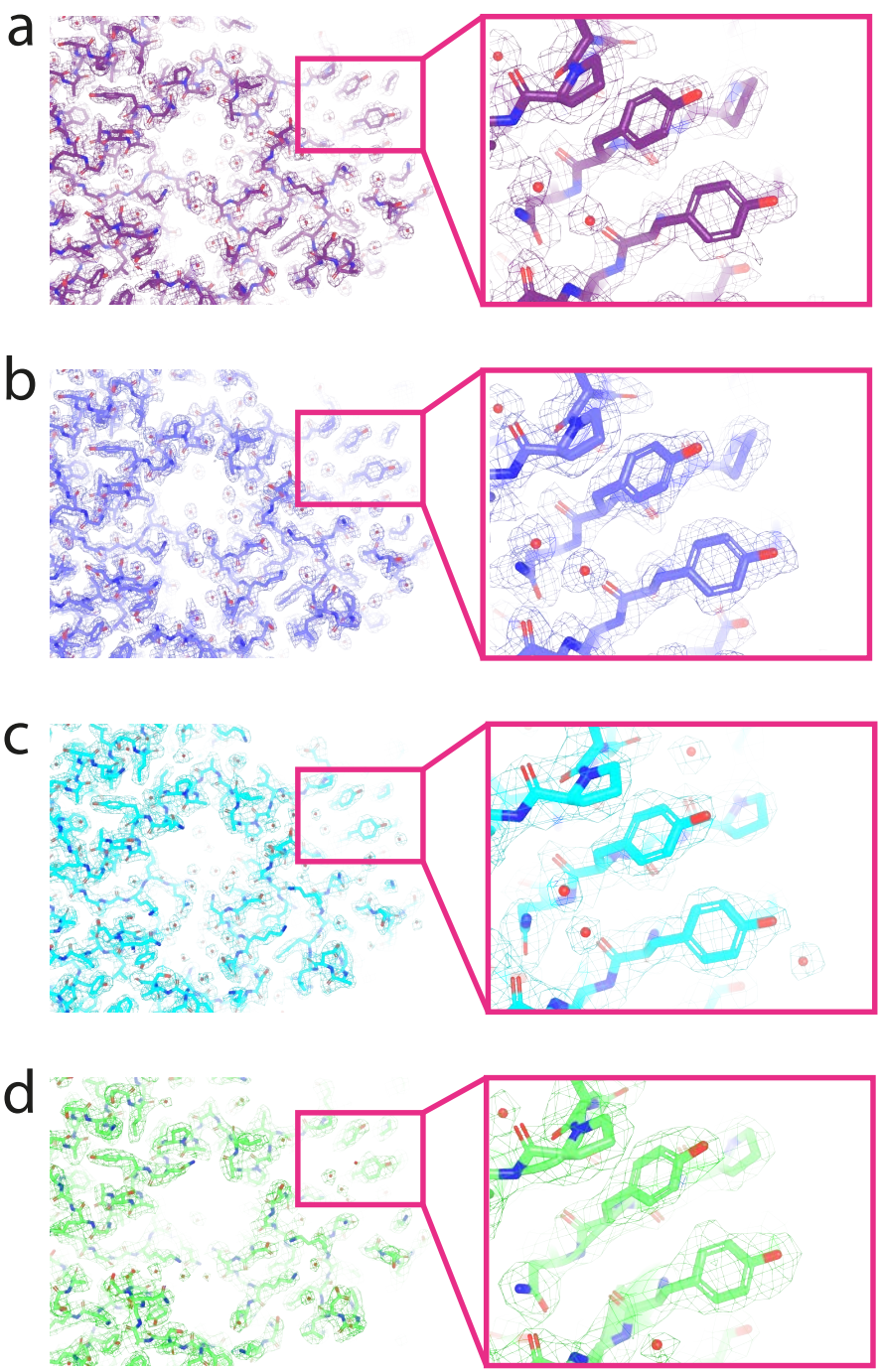

Fig. 5: SerialED affords determination of the Cry11Aa structure at a higher resolution than both SFX and 3DED. Models and electron density maps derived from the SerialED (a,b), SFX (c) and 3DED (d) dataset. In all cases, the right panel shows a close-up view of a region in the left panel. The SerialED map in (a) and (b) were calculated from the datasets with isotropic and anisotropic cutoff, respectively. Both maps were produced using the Buster-specific map-coefficients 2FOFCWT_aniso_fill and PH2FOFCWT_aniso_fill, which take into account the anisotropy of the data.

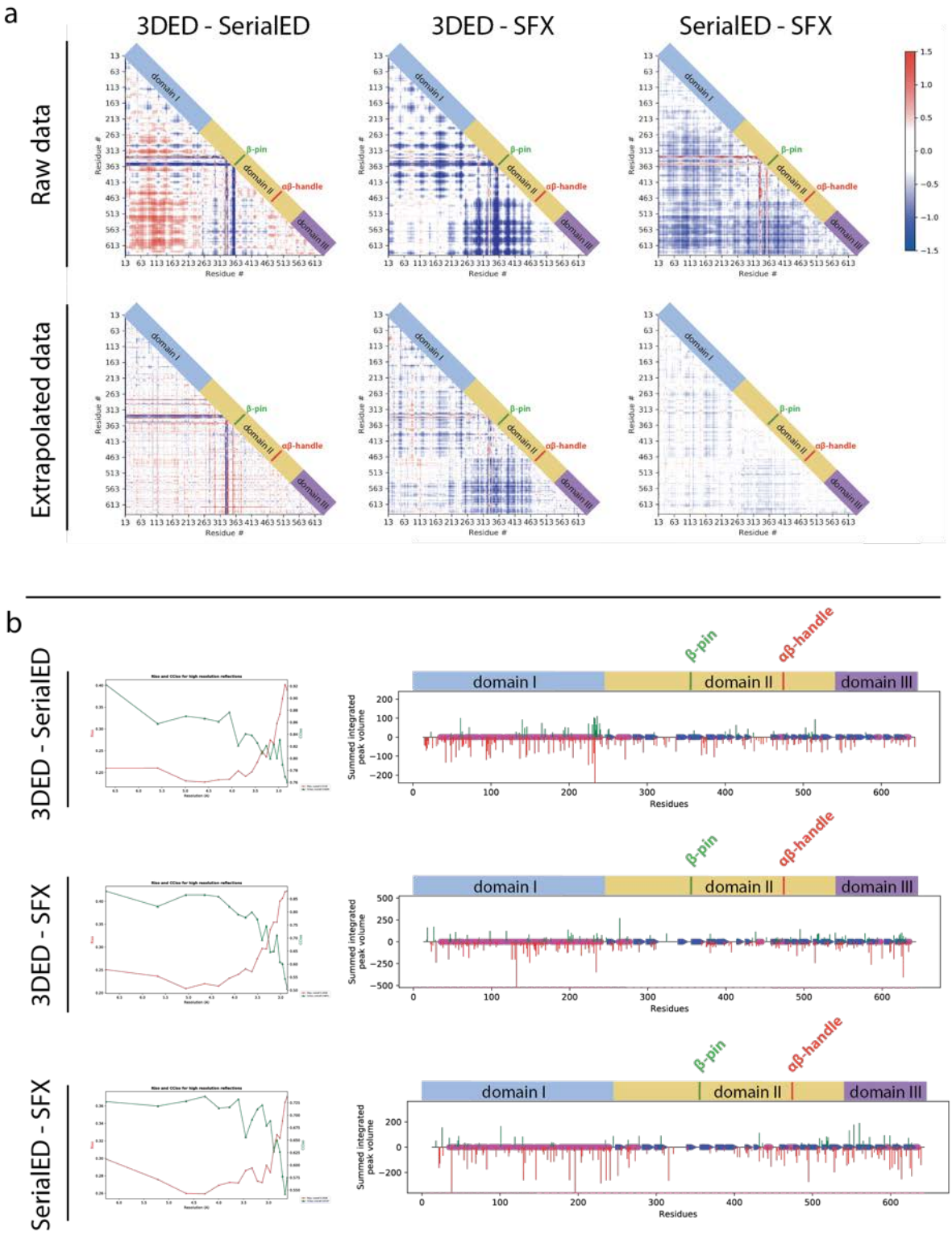

Fig. 6: Models derived by 3DED, SerialED and SFX show subtle strucural differences that point to increased disorder in the 3DED and SerialED datasets compared to the SFX dataset. a) Difference (Cα)-distance matrices comparing the 3DED and SerialED Cry11Aa structures (left), the 3DED and SFX structures(middle), and the SerialED and SFX structures (right), respectively. b) The three compared datasets are isomorphous to one another (left panels), making the calculation and interpretation of Fourier difference maps a valuable tool to obtain insights into structural differences. In the three cases (3DED vs. Serial

ED; 3DED vs. SFX; SerialED vs. SFX), we observe larger loss of electron density (negative peaks) than gain of electron density (positive peaks) indicating increasing disorder in the crystals upon cumulative electron damage or vitrification to 100 K. Also in the three cases, we see more peaks on domain I than on the other domains. We note, however, that larger peaks are seen on domain III in the $Fobs^{SerialED}$-$Fobs^{SFX}$ map.

References

1. Höfte, H. & Whiteley, H. R. Insecticidal crystal proteins of Bacillus thuringiensis. *Microbiol. Rev.* **53**, 242–255 (1989).
2. Schnepf, E. *et al.* Bacillus thuringiensis and Its Pesticidal Crystal Proteins. *Microbiol. Mol. Biol. Rev.* **62**, 775–806 (1998).
3. Bravo, A., Likitvivatanavong, S., Gill, S. S. & Soberón, M. *Bacillus thuringiensis*: A story of a successful bioinsecticide. *Insect Biochem. Mol. Biol.* **41**, 423–431 (2011).
4. Yamamoto, T. Engineering of Bacillus thuringiensis insecticidal proteins. *J. Pestic. Sci.* **47**, 47–58 (2022).
5. Bravo, A., Gill, S. S. & Soberón, M. Mode of action of *Bacillus thuringiensis* Cry and Cyt toxins and their potential for insect control. *Toxicon* **49**, 423–435 (2007).
6. Byrne, M. J. *et al.* Cryo-EM structures of an insecticidal Bt toxin reveal its mechanism of action on the membrane. *Nat. Commun.* **12**, 2791 (2021).
7. Aronson, A. I. & Shai, Y. Why Bacillus thuringiensis insecticidal toxins are so effective: unique features of their mode of action. *FEMS Microbiol. Lett.* **195**, 1–8 (2001).
8. Vachon, V., Laprade, R. & Schwartz, J.-L. Current models of the mode of action of *Bacillus thuringiensis* insecticidal crystal proteins: A critical review. *J. Invertebr. Pathol.* **111**, 1–12 (2012).
9. Li, J., Koni, P. A. & Ellar, D. J. Structure of the Mosquitocidal δ-Endotoxin CytB fromBacillus thuringiensissp.kyushuensisand Implications for Membrane Pore Formation. *J. Mol. Biol.* **257**, 129–152 (1996).
10. Boonserm, P., Ellar, D. J. & Li, J. Crystallization and preliminary X-ray diffraction studies of a mosquito-larvicidal toxin from Bacillus thuringiensis subsp. israelensis. *Acta Crystallogr. D Biol. Crystallogr.* **59**, 591–594 (2003).

11. Li, J., Carroll, J. & Ellar, D. J. Crystal structure of insecticidal δ-endotoxin from Bacillus thuringiensis at 2.5 Å resolution. *Nature* **353**, 815–821 (1991).

12. Evdokimov, A. G. *et al.* Structure of the full-length insecticidal protein Cry1Ac reveals intriguing details of toxin packaging into in vivo formed crystals. *Protein Sci.* **23**, 1491–1497 (2014).

13. Xu, C. *et al.* Crystal structure of Cry51Aa1: A potential novel insecticidal aerolysin-type β-pore-forming toxin from *Bacillus thuringiensis*. *Biochem. Biophys. Res. Commun.* **462**, 184–189 (2015).

14. Tetreau, G. *et al.* Serial femtosecond crystallography on in vivo-grown crystals drives elucidation of mosquitocidal Cyt1Aa bioactivation cascade. *Nat. Commun.* **11**, 1153 (2020).

15. Tanaka, J. *et al.* Crystal structure of the *in-cell* Cry1Aa purified from *Bacillus thuringiensis*. *Biochem. Biophys. Res. Commun.* **685**, 149144 (2023).

16. Chapman, H. N. *et al.* Femtosecond X-ray protein nanocrystallography. *Nature* **470**, 73–77 (2011).

17. Sawaya, M. R. *et al.* Protein crystal structure obtained at 2.9 A resolution from injecting bacterial cells into an X-ray free-electron laser beam. *Proc. Natl. Acad. Sci.* **111**, 12769–12774 (2014).

18. Tetreau, G. *et al.* De novo determination of mosquitocidal Cry11Aa and Cry11Ba structures from naturally-occurring nanocrystals. *Nat. Commun.* **13**, 4376 (2022).

19. Williamson, L. J. *et al.* Structure of the Lysinibacillus sphaericus Tpp49Aa1 pesticidal protein elucidated from natural crystals using MHz-SFX. *Proc. Natl. Acad. Sci.* **120**, e2203241120 (2023).

20. Colletier, J.-P. *et al.* De novo phasing with X-ray laser reveals mosquito larvicide BinAB structure. *Nature* **539**, 43–47 (2016).

21. Wiedorn, M. O. *et al.* Megahertz serial crystallography. *Nat. Commun.* **9**, 4025 (2018).

22. DePonte, D. P. *et al.* Gas dynamic virtual nozzle for generation of microscopic droplet streams. *J. Phys. Appl. Phys.* **41**, 195505 (2008).

23. Sierra, R. G. *et al.* Concentric-flow electrokinetic injector enables serial crystallography of ribosome and photosystem II. *Nat. Methods* **13**, 59–62 (2016).

24. Sierra, R. G. *et al.* Nanoflow electrospinning serial femtosecond crystallography. *Acta Crystallogr. D Biol. Crystallogr.* **68**, 1584–1587 (2012).

25. Tenboer, J. *et al.* Time-resolved serial crystallography captures high-resolution intermediates of photoactive yellow protein. *Science* **346**, 1242–1246 (2014).

26. Ishigami, I. *et al.* Structural insights into functional properties of the oxidized form of cytochrome c oxidase. *Nat. Commun.* **14**, 5752 (2023).

27. Coquelle, N. *et al.* Chromophore twisting in the excited state of a photoswitchable fluorescent protein captured by time-resolved serial femtosecond crystallography. *Nat. Chem.* **10**, 31–37 (2018).

28. Gemmi, M. & Lanza, A. E. 3D electron diffraction techniques. *Acta Crystallogr. Sect. B Struct. Sci. Cryst. Eng. Mater.* **75**, 495–504 (2019).

29. Saha, A., Nia, S. S. & Rodríguez, J. A. Electron Diffraction of 3D Molecular Crystals. *Chem. Rev.* **122**, 13883–13914 (2022).

30. Shi, D., Nannenga, B. L., Iadanza, M. G. & Gonen, T. Three-dimensional electron crystallography of protein microcrystals. *eLife* **2**, e01345 (2013).

31. Shi, D. *et al.* The collection of MicroED data for macromolecular crystallography. *Nat. Protoc.* **11**, 895–904 (2016).

32. Bernal, J. D. On the interpretation of X-ray, single crystal, rotation photographs. *Proc. R. Soc. Lond. Ser. Contain. Pap. Math. Phys. Character* **113**, 117–160 (1926).

33. Henderson, R. The potential and limitations of neutrons, electrons and X-rays for atomic resolution microscopy of unstained biological molecules. *Q. Rev. Biophys.* **28**, 171–193 (1995).

34. Jones, C. G. *et al.* The CryoEM Method MicroED as a Powerful Tool for Small Molecule Structure Determination. *ACS Cent. Sci.* **4**, 1587–1592 (2018).

35. Bruhn, J. F. *et al.* Small Molecule Microcrystal Electron Diffraction for the Pharmaceutical Industry–Lessons Learned From Examining Over Fifty Samples. *Front. Mol. Biosci.* **8**, (2021).

36. Klar, P. B. *et al.* Accurate structure models and absolute configuration determination using dynamical effects in continuous-rotation 3D electron diffraction data. *Nat. Chem.* 1–8 (2023) doi:10.1038/s41557-023-01186-1.

37. Rodriguez, J. A. *et al.* Structure of the toxic core of α-synuclein from invisible crystals. *Nature* **525**, 486–490 (2015).

38. Gallagher-Jones, M. *et al.* Sub-ångström cryo-EM structure of a prion protofibril reveals a polar clasp. *Nat. Struct. Mol. Biol.* 1 (2018) doi:10.1038/s41594-017-0018-0.

39. Hughes, M. P. *et al.* Atomic structures of low-complexity protein segments reveal kinked β sheets that assemble networks. *Science* **359**, 698–701 (2018).

40. de la Cruz, M. J. *et al.* Atomic-resolution structures from fragmented protein crystals with the cryoEM method MicroED. *Nat. Methods* **14**, 399–402 (2017).

41. Xu, H. *et al.* Solving a new R2lox protein structure by microcrystal electron diffraction. *Sci. Adv.* **5**, eaax4621 (2019).

42. Martynowycz, M. W. *et al.* MicroED structure of the human adenosine receptor determined from a single nanocrystal in LCP. *Proc. Natl. Acad. Sci.* **118**, e2106041118 (2021).

43. Hattne, J. *et al.* Analysis of Global and Site-Specific Radiation Damage in Cryo-EM. *Structure* **26**, 759-766.e4 (2018).

44. Ophus, C. Four-Dimensional Scanning Transmission Electron Microscopy (4D-STEM): From Scanning Nanodiffraction to Ptychography and Beyond. *Microsc. Microanal.* **25**, 563–582 (2019).

45. Bücker, R. *et al.* Serial protein crystallography in an electron microscope. *Nat. Commun.* **11**, 1–8 (2020).

46. Hogan-Lamarre, P., Luo, Y., Bücker, R., Miller, R. J. D. & Zou, X. STEM SerialED: achieving high-resolution data for ab initio structure determination of beam-sensitive nanocrystalline materials. *IUCrJ* **11**, 62–72 (2024).

47. Gallagher-Jones, M. *et al.* Atomic structures determined from digitally defined nanocrystalline regions. *IUCrJ* **7**, 490–499 (2020).

48. Gallagher-Jones, M. *et al.* Nanoscale mosaicity revealed in peptide microcrystals by scanning electron nanodiffraction. *Commun. Biol.* **2**, 1–8 (2019).

49. Martynowycz, M. W., Clabbers, M. T. B., Hattne, J. & Gonen, T. Ab initio phasing macromolecular structures using electron-counted MicroED data. *Nat. Methods* **19**, 724–729 (2022).

50. Hattne, J., Clabbers, M. T. B., Martynowycz, M. W. & Gonen, T. Electron counting with direct electron detectors in MicroED. *Structure* **31**, 1504-1509.e1 (2023).

51. Abramson, J. *et al.* Accurate structure prediction of biomolecular interactions with AlphaFold 3. *Nature* **630**, 493–500 (2024).

52. Yonekura, K., Maki-Yonekura, S. & Namba, K. Quantitative Comparison of Zero-Loss and Conventional Electron Diffraction from Two-Dimensional and Thin Three-Dimensional Protein Crystals. *Biophys. J.* **82**, 2784–2797 (2002).

53. Yonekura, K., Ishikawa, T. & Maki-Yonekura, S. A new cryo-EM system for electron 3D crystallography by eEFD. *J. Struct. Biol.* **206**, 243–253 (2019).

54. Clabbers, M. T. B., Hattne, J., Martynowycz, M. W. & Gonen, T. Energy filtering enables macromolecular MicroED data at sub-atomic resolution. *Nat. Commun.* **16**, 2247 (2025).

55. Smeets, S., Zou, X. & Wan, W. Serial electron crystallography for structure determination and phase analysis of nanocrystalline materials. *J. Appl. Crystallogr.* **51**, 1262–1273 (2018).

56. Coquelle, N. *et al.* Raster-scanning serial protein crystallography using micro- and nano-focused synchrotron beams. *Acta Crystallogr. D Biol. Crystallogr.* **71**, 1184–1196 (2015).

57. Sherrell, D. A. *et al.* A modular and compact portable mini-endstation for high-precision, high-speed fixed target serial crystallography at FEL and synchrotron sources. *J. Synchrotron Radiat.* **22**, 1372–1378 (2015).

58. Oghbaey, S. *et al.* Fixed target combined with spectral mapping: approaching 100% hit rates for serial crystallography. *Acta Crystallogr. Sect. Struct. Biol.* **72**, 944–955 (2016).

59. White, T. A. *et al.* CrystFEL: a software suite for snapshot serial crystallography. *J. Appl. Crystallogr.* **45**, 335–341 (2012).

60. Gevorkov, Y. *et al.* pinkIndexer – a universal indexer for pink-beam X-ray and electron diffraction snapshots. *Acta Crystallogr. Sect. Found. Adv.* **76**, 121–131 (2020).

61. Vonrhein, C. *et al.* Advances in automated data analysis and processing within ıt autoPROC, combined with improved characterisation, mitigation and visualisation of the anisotropy of diffraction limits using ıt STARANISO. *Acta Crystallogr. Sect. A* **74**, a360 (2018).

62. Schneider, T. R. Objective comparison of protein structures: error--scaled difference distance matrices. *Acta Crystallogr. D Biol. Crystallogr.* **56**, 714–721 (2000).

63. De Zitter, E., Coquelle, N., Oeser, P., Barends, T. R. M. & Colletier, J.-P. Xtrapol8 enables automatic elucidation of low-occupancy intermediate-states in crystallographic studies. *Commun. Biol.* **5**, 1–11 (2022).

64. Yonekura, K., Kato, K., Ogasawara, M., Tomita, M. & Toyoshima, C. Electron crystallography of ultrathin 3D protein crystals: Atomic model with charges. *Proc. Natl. Acad. Sci.* **112**, 3368–3373 (2015).

65. Bücker, R., Hogan-Lamarre, P. & Miller, R. J. D. Serial Electron Diffraction Data Processing With diffractem and CrystFEL. *Front. Mol. Biosci.* **8**, (2021).

66. Wolff, A. M. *et al.* Comparing serial X-ray crystallography and microcrystal electron diffraction (MicroED) as methods for routine structure determination from small macromolecular crystals. *IUCrJ* **7**, 306–323 (2020).

67. Clabbers, M. T. B. *et al.* MyD88 TIR domain higher-order assembly interactions revealed by microcrystal electron diffraction and serial femtosecond crystallography. *Nat. Commun.* **12**, 2578 (2021).

68. Parkhurst, J. M. *et al.* Investigation of the milling characteristics of different focused-ion-beam sources assessed by three-dimensional electron diffraction from crystal lamellae. *IUCrJ* **10**, 270–287 (2023).

69. Klar, P. B. *et al.* Cryo-tomography and 3D Electron Diffraction Reveal the Polar Habit and Chiral Structure of the Malaria Pigment Crystal Hemozoin. *ACS Cent. Sci.* (2024) doi:10.1021/acscentsci.4c00162.

70. Yang, J. E., Mitchell, J. M., Bingman, C. A., Mosher, D. F. & Wright, E. R. In situ crystalline structure of the human eosinophil major basic protein-1. 2024.10.09.617336 Preprint at https://doi.org/10.1101/2024.10.09.617336 (2024).

71. Martynowycz, M. W. *et al.* A robust approach for MicroED sample preparation of lipidic cubic phase embedded membrane protein crystals. *Nat. Commun.* **14**, 1086 (2023).

72. Berger, C. *et al.* Plasma FIB milling for the determination of structures in situ. *Nat. Commun.* **14**, 629 (2023).

73. Soragni, A. *et al.* Toxicity of Eosinophil MBP Is Repressed by Intracellular Crystallization and Promoted by Extracellular Aggregation. *Mol. Cell* **57**, 1011–1021 (2015).

74. Peng, R. *et al.* Characterizing the resolution and throughput of the Apollo direct electron detector. *J. Struct. Biol. X* **7**, 100080 (2023).

75. Vlahakis, N. *et al.* Fast event-based electron counting for small molecule structure determination by MicroED. Preprint at https://doi.org/10.26434/chemrxiv-2024-p24xf (2024).

76. Zhao, J. *et al.* A simple pressure-assisted method for MicroED specimen preparation. *Nat. Commun.* **12**, 5036 (2021).

77. Shoeman, R. L., Hartmann, E. & Schlichting, I. Growing and making nano- and microcrystals. *Nat. Protoc.* **18**, 854–882 (2023).

78. Nicolas, W. J. *et al.* Comprehensive microcrystal electron diffraction sample preparation for cryo-EM. *Nat. Protoc.* 1–35 (2024) doi:10.1038/s41596-024-01088-7.

79. Truong, K.-N. *et al.* Making the Most of 3D Electron Diffraction: Best Practices to Handle a New Tool. *Symmetry* **15**, 1555 (2023).

80. Wu, D. & Federici, B. A. Improved production of the insecticidal CryIVD protein in Bacillus thuringiensis using cryIA(c) promoters to express the gene for an associated 20-kDa protein. *Appl. Microbiol. Biotechnol.* **42**, 697–702 (1995).

81. Mastronarde, D. N. Automated electron microscope tomography using robust prediction of specimen movements. *J. Struct. Biol.* **152**, 36–51 (2005).

82. Winter, G. *et al.* DIALS as a toolkit. *Protein Sci. Publ. Protein Soc.* **31**, 232 (2021).

83. Vypritskaia, A., Zou, X., Yang, T. & Waterman, D. G. How to use DIALS to process chemical crystallography 3D ED rotation data from pixel array detectors. *Acta Crystallogr. Sect. C Struct. Chem.* **81**, 1–13 (2025).

84. Gildea, R. J. *et al.* xia2.multiplex: a multi-crystal data-analysis pipeline. *Acta Crystallogr. Sect. Struct. Biol.* **78**, 752–769 (2022).

85. Liebschner, D. *et al.* Macromolecular structure determination using X-rays, neutrons and electrons: recent developments in Phenix. *Acta Crystallogr. Sect. Struct. Biol.* **75**, 861–877 (2019).

86. McCoy, A. J. *et al.* Phaser crystallographic software. *J. Appl. Crystallogr.* **40**, 658–674 (2007).

87. Emsley, P., Lohkamp, B., Scott, W. G. & Cowtan, K. Features and development of Coot. *Acta Crystallogr. D Biol. Crystallogr.* **66**, 486–501 (2010).

88. White, T. A. *et al.* Recent developments in CrystFEL. *J. Appl. Crystallogr.* **49**, 680–689 (2016).

89. White, T. A. Processing of XFEL Data. in *Protein Crystallography: Methods and Protocols* (eds. Wlodawer, A., Dauter, Z. & Jaskolski, M.) 325–347 (Springer, New York, NY, 2017). doi:10.1007/978-1-4939-7000-1_13.

90. Gérard Bricogne *et al.* BUSTER. Global Phasing Ltd. (2017).

91. Goddard, T. D. *et al.* UCSF ChimeraX: Meeting modern challenges in visualization and analysis. *Protein Sci. Publ. Protein Soc.* **27**, 14–25 (2018).